

1 **IITM High-Resolution Global Forecast Model Version 1: An attempt**
2 **to resolve monsoon prediction deadlock**

3 R. Phani Murali Krishna¹, Siddharth Kumar¹, A. Gopinathan Prajeesh², Peter Bechtold³, Nils Wedi³,
4 Kumar Roy⁴, Malay Ganai¹, B. Revanth Reddy¹, Snehlata Tirkey¹, Tanmoy Goswami¹, Radhika
5 Kanase¹, Sahadat Sarkar¹, Medha Deshpande¹, Parthasarathi Mukhopadhyay^{1,5}
6

7 ¹Indian Institute of Tropical Meteorology, Ministry of Earth Sciences, Dr. Homi Bhabha Road, Pune 411008, India

8 ² King Abdullah University of Science and Technology, Saudi Arabia

9 ³ ECMWF

10 ⁴ University of Victoria, Canada

11 ⁵ Department of Earth and Environmental Sciences, Indian Institute of Science Education and Research, Berhampur 760003,
12 Odisha, India
13

14

15

16 *Correspondence to:* Dr. P. Mukhopadhyay (mpartha@tropmet.res.in; parthasarathi64@gmail.com)

17

18

19

20

21

22

23

24

25

26

27

28 **Abstract.** The prediction of Indian monsoon rainfall variability affecting a country with a population of billions remained
29 one of the major challenges of the numerical weather prediction community. While in recent years, there has been a
30 significant improvement in predicting the synoptic scale transients associated with the monsoon circulation, the intricacies of
31 rainfall variability remained a challenge. Here, an attempt is made to develop a global model using a dynamic core of a cubic
32 octahedral grid that provides a higher resolution of 6.5 km over the global tropics. This high-resolution model has been
33 developed to resolve the monsoon convection. Reforecasts with the IITM High-resolution Global Forecast Model (HGFM)
34 have been run daily from June through September 2022. The HGFM model has a wave number truncation of 1534 in the
35 cubic octahedral grid. The monsoon events have been predicted with a ten-day lead time. The HGFM model is compared to
36 the operational GFS T1534. While the HGFM provides skills comparable to the GFS, it shows better skills for higher
37 precipitation thresholds. This model is currently being run in experimental mode and will be made operational.

38

39

40

41

42

43

44

45

46

47

48

49

50

51

52

53

54

55 1 Introduction

56 In spite of significant improvement in numerical weather prediction skill in the last decades (Bechtold et al., 2008;
57 Magnusson and Kallen 2013; Hoffman et al., 2018) predictions of tropical rainfall variability remain a challenge (Westra et
58 al., 2014; Prakash et al., 2016). Stephens et al. (2010) demonstrated that the models predict in the tropics too many rainy
59 days which are in the lighter rain category. The challenges of tropical rainfall variability have also been demonstrated by
60 Watson et al., 2017. The vagaries of the Indian monsoon every year affect the lifestyle of billions of people and the economy
61 of the Indian sub-continent modulating its Gross Domestic Product (GDP) (Gadgil and Gadgil, 2006). It is therefore of the
62 utmost importance to improve the weather prediction skill in general and extreme precipitation events in particular. With the
63 increase of computing power, the resolution of numerical weather prediction models have been increasing and global models
64 with a resolution of 1~7 km have become a reality (Majewski et al., 2002; Satoh et al., 2005; Miura et al., 2007; Staniforth
65 and Thuburn, 2012; Li et al., 2015; Satoh et al., 2019; Wedi et al., 2020). The higher resolution of Numerical Weather
66 Prediction (NWP) models has been found to produce a realistic rainfall variability across scales including diurnal variation,
67 better Madden Julian Oscillation (MJO) variability and seasonal mean climate (Kinter et al., 2013; Rajendran and Kitoh,
68 2008; Skamarock et al., 2012; Molod et al., 2015; Crueger et al. 2018; Giorgetta et al., 2018). In India, operational NWP was
69 initiated with moderate resolution of T80 and then gradually enhanced to T382, T574 (Prasad et al., 2011, 2014, 2017) and
70 very recently to T1534 (Mukhopadhyay et al., 2019). The advantage of using higher resolution (T1534~12.5 km) as against
71 the lower resolution T574 (~27 km) was found by enhancement of the model skill by 2 days (Rao et al., 2019). The National
72 Centre for Environmental Prediction (NCEP) GFS model with 21 members has been used for probabilistic forecasts since
73 June 2018 (Deshpande et al., 2021). The high-resolution GFS T1534 is found to enhance the skill of heavy rainfall event
74 (Mukhopadhyay et al., 2019), tropical cyclones and even block level prediction of rainfall (block is a sub-division of a
75 districts in India, typically of the size of the grid of GFS T1534). However, the skill of the GFS T1534 for prediction of
76 extremely heavy precipitation can still be improved particularly over the orographic regions of India such as the southern
77 coastal state of Kerala, India (Mukhopadhyay et al., 2021).

78 The 12-km deterministic and the ensemble model based on the GFS do show reasonably good skill in capturing the monsoon
79 rainfall with 3 to 5 days lead time. The skill of the GFS forecast for Indian monsoon has been reported by Mukhopadhyay et
80 al. (2019) and the skill of tropical cyclones with the Global Ensemble Forecast System (GEFS) has also been reported in
81 Deshpande et al. (2021) and Kanase et al. (2023). However, in a recent study Mukhopadhyay et al. (2021) showed that three
82 state-of-the-art ensemble forecast systems namely the GEFS, the United Kingdom Meteorological Office (UKMO) based
83 NCMRWF Ensemble Prediction System (NEPS) run by National Centre for Medium Range Weather Forecasting
84 (NCMRWF) and the Integrated Forecasting System (IFS) by ECMWF struggled to capture the extremely heavy rainfall over
85 Kerala state of India during August 2018 and August 2019 extremely heavy rainfall episode. This in fact brought up the
86 limitation of the model in resolving the rainfall variability over the Indian region and more importantly over the orographic
87 region. One of the limitations in resolving the regional variabilities of rainfall is the horizontal resolution which does not

88 allow the model to resolve the smaller scale processes. Therefore, a need was felt to enhance the horizontal resolution of the
89 existing GFS based forecasting system. As running of a model close to the convection permitting model (at a resolution
90 lesser than 10 km) is computationally too expensive in conventional linear reduced Gaussian grids, it was thought to build a
91 weather model with a grid which has a variable resolution from the pole to the equator. In view of this, the GFS linear
92 reduced Gaussian Grid at triangular truncation 1534 is replaced by an equivalent truncation of 1534 in triangular cubic
93 octahedral (Tco) grid. The equivalent model resolutions of the linear T1534 and the cubic Tco1534 grids are displayed in
94 Fig. 1a. Indeed, as the linear grid has a roughly uniform grid point resolution of 12.5 km the octahedral grid has a resolution
95 of about 8 km in the Polar Regions and around 6 km in the tropical band. One of the prominent examples of the Global NWP
96 model with the Tco grid is that of the European Centre for Medium-Range Weather Forecasts (ECMWF) model suites. The
97 Tco grid provides several advantages (ECMWF Documentation Cy43r1, 2016) over that of the conventional reduced
98 Gaussian linear grid (Fig. 1a), to name a few- significant reduction in computation cost, improved representation of
99 orography, better filtering and better conservation properties. These properties of Tco make it a better candidate, particularly
100 for the utilization of high-performance computers (HPC).

101 This paper is the first attempt to best of our knowledge, towards building a model close to a convection permitting global
102 weather model in India with an emphasis to Indian monsoon rainfall variability. The details of the model development and
103 the experiments conducted have been elaborated in Sect. 2. The model results are analysed in Sect. 3, and the conclusion of
104 the study is summarized in Sect. 4.

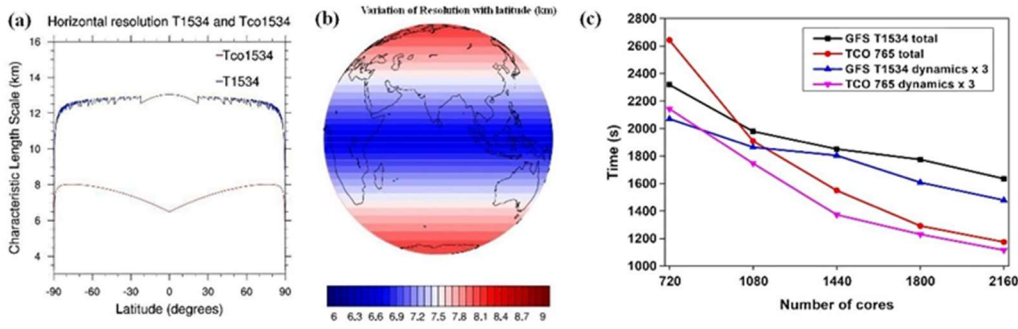
105 **2 Model, Data and Methodology**

106 This new grid, namely the Triangular Cubic Octahedral (Tco) grid, has been adopted to change the existing GFS (semi-
107 lagrangian) Gaussian linear model system. In the spectral domain, dynamical fields are represented by the sum of spherical
108 harmonics. The total wavenumber characterizes the spherical harmonics, and the associated wavelength is the ratio of the
109 circumference of the Earth to the total wavenumber. The value of the maximum wavenumber (n_{max}) used to represent a
110 field as the sum of spherical harmonics is also the spectral truncation of the model. In the case of both GFS and Tco, the
111 value of n_{max} is 1534. For the same spectral truncation n_{max} , the number of latitude circles from the equator to the pole
112 can vary depending on the choice of spectral transformation. For a linear grid, $n_{max}=2N-1$, and for a cubic grid, $n_{max}=N-$
113 1 . Therefore, for a linear Gaussian grid, the smallest wavelength is represented by only two grid points, as is the case with
114 the GFS 1534 model. However, in the case of triangular truncation, the smallest wavelength is represented by four grid
115 points (in the case of the Tco grid). In triangular truncation, for the same spectral truncation, the number of latitude circles is
116 about double that of the linear truncation. For the GFS model, the horizontal resolution is ~ 12.5 km, and applying the cubic
117 grid ensures that the horizontal resolution becomes ~ 6.5 km in the tropics (about half of the currently used model resolution)
118 for the Tco grid. In the Tco grid, the number of latitude circles is 1535.

119 Once a particular choice of spectral truncation is made, the number of latitude circles becomes obvious. However, the
120 number of longitude circles per latitude circle remains to be prescribed for the creation of the global grid structure. In a fully
121 Gaussian grid, the number of longitude circles per latitude circle remains the same throughout the latitudes from the equator
122 to the pole. Thus, the effective resolution near the poles becomes very high compared to the equatorial regions. This specific
123 requirement demands too many computational resources and poses problems of numerical instability. To overcome that, in
124 the linear Gaussian grid, the number of latitude circles decreases in a certain way from the equator toward the pole to ensure
125 almost the same zonal resolution. For the cubic octahedral grid, the number of longitude points per latitude circle is
126 prescribed in a different way. The latitude circle closest to the pole consists of 20 longitude points, and the number of
127 longitude points increases by 4 at each latitude circle, moving from poles towards the equator. The number of longitude
128 points at the equator in the case of the Tco grid is given by $N_x=20+1534*4=6156$. Therefore, the zonal grid
129 length= $2\pi*R/N_x\sim 6.5$ km. In the original reduced Gaussian grid, the number of longitude points per latitude remains fixed in
130 different blocks of latitudes. The number of latitude points jumps from one block to the other by a constant number. Unlike
131 the linear reduced Gaussian grid, the horizontal resolution varies more smoothly with latitudes in Tco. The Collignon
132 projection of a sphere obtains this configuration onto an octahedron. In the current study, the Tco grid at truncation
133 wavenumber of 1534 is being used. This new version of the model is mentioned as HGFM (High-resolution Global Forecast
134 Model Version 1) throughout the manuscript. Fig. 1a and Fig. 1b depicts the variation of grid resolution with latitude in the
135 GFS (SL) and HGFM (Tco).

136 Before testing the HGFM with complete physics (see Table 1 for description of physics being used in both versions of
137 model), we have made a version of HGFM with only a dynamical core following Held and Suarez (1994), referred to as
138 HS94. The HS94 is run to check the stability of the Tco grid framework. Surface boundary conditions for the Tco grid have
139 been meticulously prepared to ensure the accuracy of grid-point representation. Moreover, the HGFM (Tco1534) has been
140 developed with complete physics and incorporates essential boundary conditions, including global topography, global land-
141 use-land-cover etc. The HGFM at Tco1534 truncation is depicted over the globe in Fig. 1. The model has been run daily for
142 ten days forecast at IITM Pratyush HPC system. To understand the computational efficiency of Tco model, time taken for
143 one day forecast is compared for GFS 1534 and HGFM model (Tco 765 in this case) (see Fig. 1c). A comparison between
144 GFS 1534 and Tco 765 is made because both models have almost same number of grid points. It is clear that Tco 765
145 significantly saves the runtime in dynamical core and total time as well. Moreover, the Tco model is in general more scalable
146 for higher number of cores (not shown). The model has been run since 2022 and here the analyses for the summer monsoon
147 season of June, July, August and September (JJAS) 2022 are being presented. A detailed analysis of the model run is
148 discussed in the results section. Apart from the monsoon season (JJAS 2022), few case studies are also discussed.

149



150

151 **Figure 1. Variation of grid length with latitude in GFS (blue) and Tco (red) (a), depiction of grid resolution over the globe in Tco**
 152 **grid (b), total and dynamics time taken for different number of cores (c). Time taken by GFS and HGFM for one day forecast**
 153 **(Left vertical axis is total time taken and model dynamics time multiplied by 3).**

154 To verify the model forecast, the daily observed gridded rainfall data from the Integrated Multi-satellite Retrievals for GPM
 155 (IMERG) version 06B (Huffman et al., 2019) rainfall data at $0.1^\circ \times 0.1^\circ$ (10 km) horizontal resolution is utilized for the year
 156 of 2022 for JJAS season. Additionally, to validate a heavy rainfall event over India, gridded rainfall from India
 157 Meteorological Department (IMD) at 25 km resolution is used. The IMD rainfall data are merged product of gridded rain
 158 gauge observations and GPM satellite-estimated rainfall over the ISM region (Mitra et al., 2014). Further, the reanalysis-
 159 based parameters from the fifth generation of ECMWF atmospheric reanalyses (ERA5) products (Hersbach and Dee, 2016)
 160 are utilized at 25 km horizontal resolution during JJAS of the year 2022.

161 **Table 1. Details of domain configuration and physics options used in HGFM.**

Physics	Description
Radiation	Rapid Radiative Transfer Model (RRTM) for both Shortwave and Longwave (Iacono et al., 2000; Clough et al., 2005) with Monte Carlo Independent Column Approximation (McICA)
Microphysics	Formulated grid-scale condensation and precipitation (Sundqvist et al., 1989; Zhao and Carr, 1997)
Convection	Aerosol aware and Mass flux based Simplified Arakawa-Schubert (SAS) shallow convection (Pan and Wu, 1995; Han and Pan, 2011; Arakawa and Wu, 2013; Han et al., 2017)
Planetary Boundary Layer (PBL)	Hybrid Eddy-Diffusivity Mass Flux vertical turbulent mixing scheme (Han and Pan, 2011; Han et al., 2016)
Gravity Wave Drag (GWD)	Mountain blocking (Alpert et al., 1988; Kim and Arakawa, 1995; Lott and Miller, 1997) and stationary convective-forced GWD (Chun and Baik, 1998)

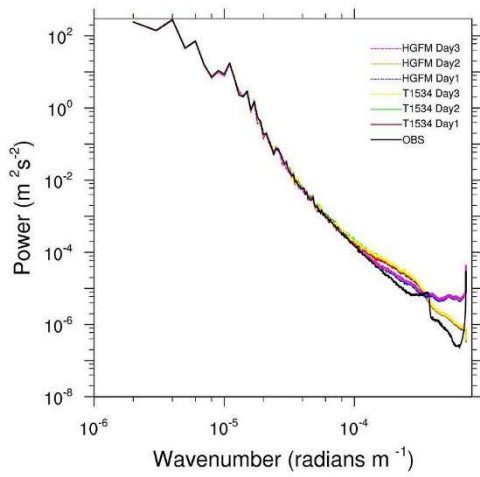
162

163 3 Results and Discussions

164 3.1 200 hPa Kinetic Energy Spectra

165 Before going into the details of model validation, the first metric to evaluate the model fidelity is to validate the Kinetic
166 Energy (KE) spectra of 200 hPa wind. The KE spectra provide information about the distribution of kinetic energy across the
167 scale. A close resemblance between observed /reanalysis-based spectra and spectra produced by the model gives confidence
168 about accuracy of overall model configuration. The kinetic energy (KE) spectrum in the upper troposphere exhibits two
169 clearly defined power-law patterns. From observational studies, it is established that at large-scale, rotational modes prevail
170 (k^{-3}) while at mesoscales, divergent modes are dominant ($k^{-5/3}$) (Nastrom and Gage, 1985). Figure 2 shows the KE spectra of
171 200 hPa wind simulated by HGFM and GFS T1534. The KE spectra for the forecast up to 3 days lead time has been
172 compared with ERA5 data. While both the models reasonably capture $k^{-5/3}$ behaviour of the mesoscale at the higher
173 wavenumber, but the HGFM appears to capture the k^{-3} behaviour of the large scale at the lower wavenumber closer to
174 observation. It is observed that beyond wavenumber 10^{-4} there is slight departure of the spectra from observation specially
175 for HGFM. However, the regions of interest in KE spectra are the k^{-3} dependence for the large scale and a less steep, $k^{-5/3}$
176 dependence for the mesoscale. The tail of the spectra at higher wave numbers typically has less energy due to the dissipation
177 of kinetic energy with increase of wave number, however models tend to dissipate the energy at higher wave number at a
178 much faster rate depending on the damping used in the model (Skamarock, 2004). To keep the spectra realistic, a common
179 practice is to reduces the damping which may increase the energy at higher wavenumbers as observed in this case for
180 HGFM. However, this will not have much impact in our analysis as these are the small-scale features. The KE spectra
181 indicates that overall configuration of both versions of the model is robust. Therefore, now we turn our attention towards
182 verification of convective available potential energy and rainfall simulations, the most desirable parameter in model
183 forecasts.

184

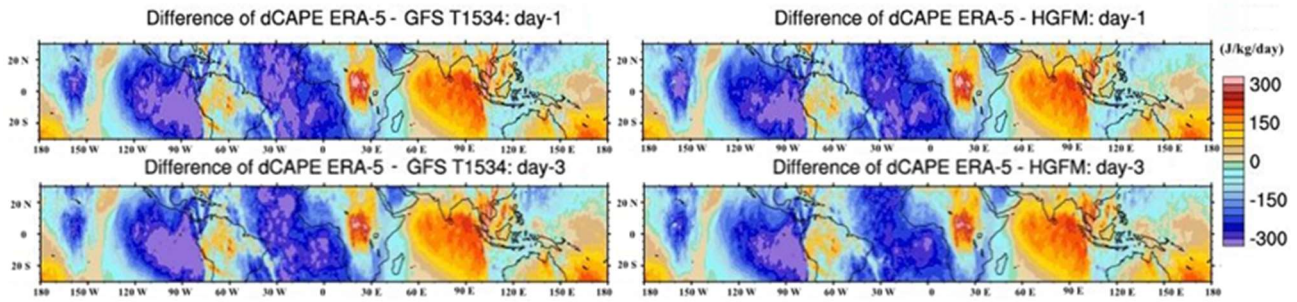


185

186 **Figure 2. Kinetic energy spectra of 200 hPa wind for observation and different lead times of GFS T1534 and HGFM.**

187 **3.2 Quasi-equilibrium in models**

188 Both model versions are run at high-resolutions, close to convection-permitting models' resolution. However, in this case, a
 189 scale-aware convection scheme is used to parameterize deep convection in the model. From observational studies it has been
 190 established that tropical atmosphere deviates significantly from the convective-quasi equilibrium (e.g., Zhang, 2003). The
 191 convective quasi-equilibrium (CQE) is the fundamental approach used in most models for parameterization of deep
 192 convection (Arakawa and Schubert 1974). To understand up to what extent both model versions obey CQE, we adopted the
 193 methodology suggested in Kumar et al. (2022). The absolute value of changes in Convective Available Potential Energy
 194 (CAPE) at daily timescales is analysed from GFS T1534 and HGFM models for the year 2022 during JJAS and compared
 195 with the ERA-5 data (Figure not shown). Notable changes were observed in the daily dCAPE values between GFS T1534
 196 and HGFM compared to ERA-5. The daily dCAPE values from ERA-5 data matches better with the HGFM than GFS T1534
 197 for day 1 and day 3 lead times. The difference of dCAPE between ERA-5 and models is presented for day-1 and day-3 lead
 198 time forecast (Fig. 3). The dCAPE difference quantified from ERA-5 with GFS T1534 were -49.0570 (J/kg/day) and $-$
 199 47.3799 (J/kg/day) for day1 and day 3 lead times respectively, similarly with HGFM -49.1278 (J/kg/day) and -43.7668
 200 (J/kg/day) for day 1 and day 3 lead times respectively.

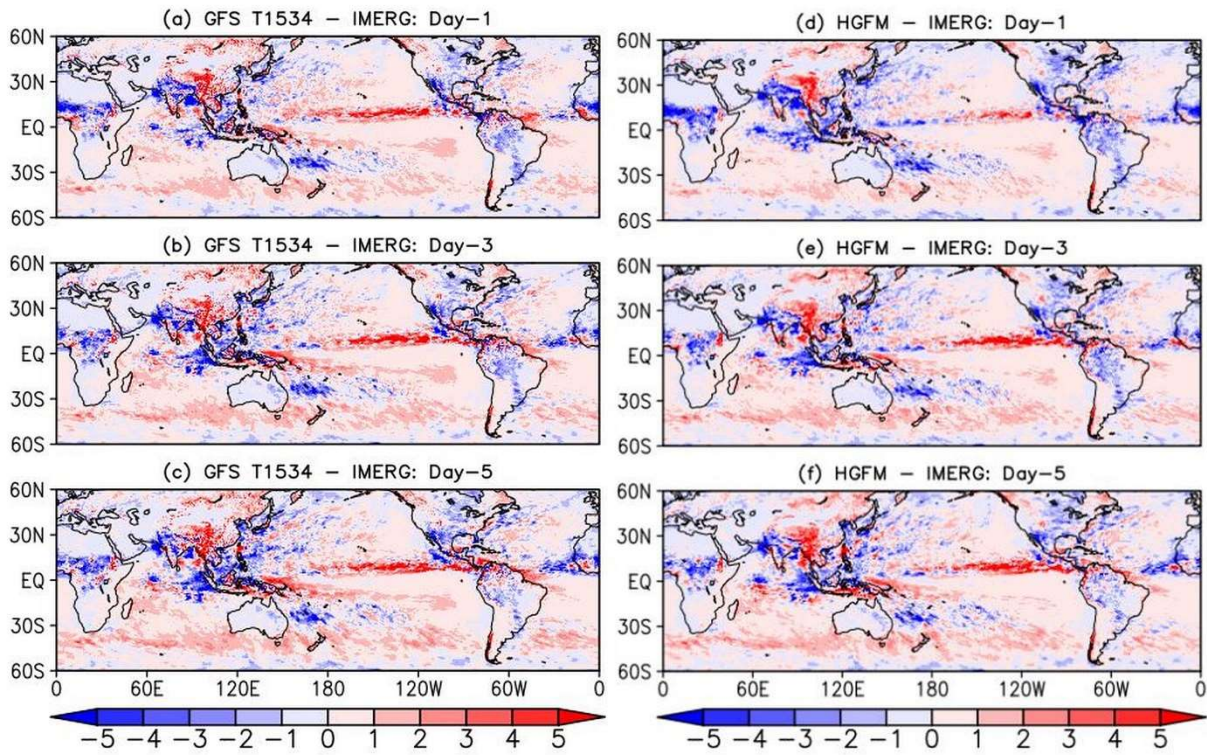


201
 202 **Figure 3. The difference of dCAPE from ERA-5 and GFS T1534 for day-1 and day-3 (left panels), and from ERA-5**
 203 **and HGFM for day-1 and day-3 (right panels).**

204 **3.3 Analysis of Global precipitation**

205 The global precipitation bias of GFS (left panel of Fig. 4 and HGFM (right panel) with respect to Integrated Multi-satellite
 206 Retrievals for GPM (IMERG) data, with day 1, day 3 and day 5 lead time is shown in Fig. 4. Both the models broadly show
 207 a similar rainfall bias over the global land and global ocean. However, there are some subtle differences. The day 1 forecast
 208 (Fig. 4a) of GFS shows a wet bias over the equatorial eastern Pacific extending up to the tropical western Pacific. On the
 209 other hand, the HGFM on day 1 lead (Fig. 4d) also shows a wet bias mostly confined over the tropical eastern Pacific and a
 210 slight negative bias over western Pacific. For HGFM, the positive bias of rainfall over the tropical ocean appears to be
 211 mostly over the eastern Pacific while that of GFS appears to be over eastern Pacific and extending towards the central and
 212 west Pacific for all the lead time. The eastern Pacific precipitation overestimation could be due to improper representation of
 213 shallow convection over the region. Raymond (2017) highlighted the complex nature of SST and associated cloudiness and
 214 convection over the region. Apart from the oceanic region, the major global land regions (central African Continent,
 215 Maritime continent, Indian summer monsoon region, northern part of South America) shows a negative bias in both the
 216 models at different lead times (Fig. 4) which is likely related to the model physical parameterizations.

217



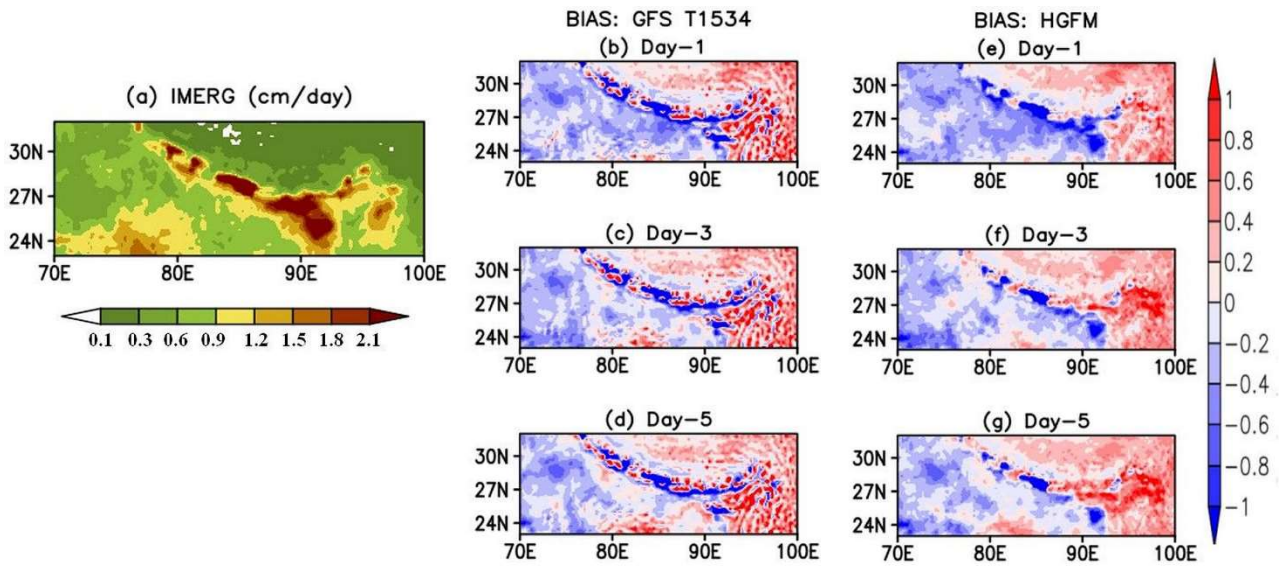
218

219 **Figure 4. Global JJAS precipitation bias (cm/day) of GFS T1534 (left panel) with respect to IMERG for (a) day-1, (b) day-3 and**
 220 **(c) day-5 lead time. Right column (d-f) indicates similar plots but for HGFM.**

221 3.4 Indian summer monsoon precipitation and related features

222 While Fig. 4 depicted the precipitation bias over the global domain, it will be interesting to investigate the model forecast
 223 performance over the complex orographic region over the Indian domain, the region of our utmost interest. As mentioned
 224 earlier, one of the major advantages of using a Tco grid is a better representation of orography. Therefore, it is imperative to
 225 investigate the forecast skill of the high resolution HGFM model over the mountainous Himalayan foothills, adjoining
 226 northeast India, and Western Ghats (WGs) region (shown in Fig. 5 and 6 respectively). The GFS T1534 model forecasts
 227 indicate spurious rainfall activity over the Himalayan foothills and northeast India region for all lead times (Fig. 5b-d). On
 228 contrary, the HGFM model with finer horizontal resolution largely resolves the spurious rainfall over the region as shown in
 229 Fig. 5e-g. The Gibbs waves are largely suppressed over the mountainous terrains in HGFM compared to GFS T1534.
 230 Similarly, the precipitation distribution over the WGs region shows considerable overestimation in GFS T1534 for all lead
 231 times (Fig. 6b-d). On the other hand, the magnitude of overestimation is decreased considerably in HGFM forecasts as
 232 depicted in Fig. 6e-g. Thus, the above analysis brings out the fact that HGFM shows its potential in predicting realistic
 233 rainfall distribution over the orographic regions.

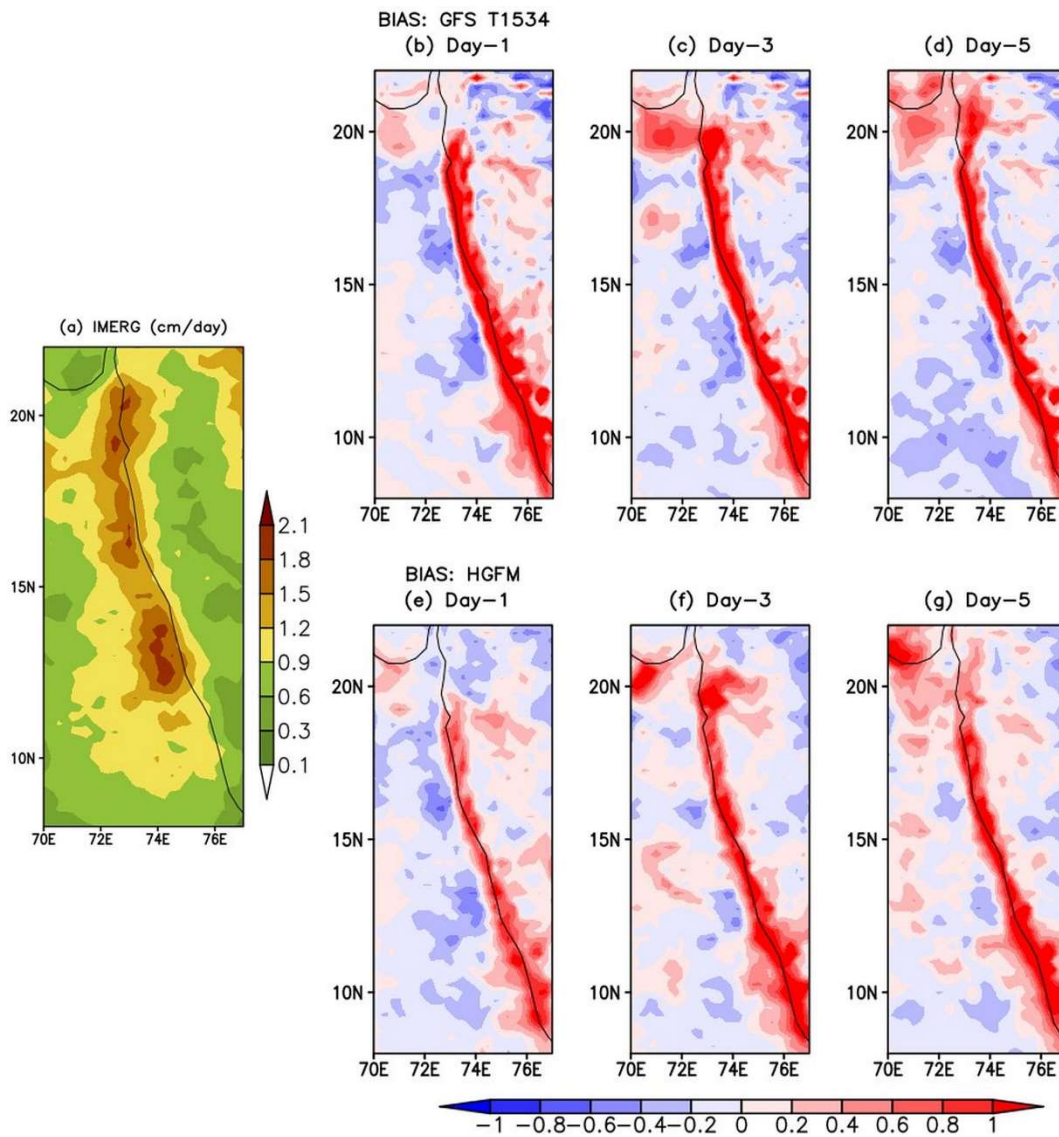
234



235

236 **Figure 5. Comparison of JJAS mean precipitation (cm/day) and Bias in IMERG data (cm/day) (a) with GFS T1534 (b, c, d) and**
 237 **TCO 1534 (e, f, g) during 2022 over Himalayan foothills and Northeast India for day-1 day-3 and day-5 lead time.**

238



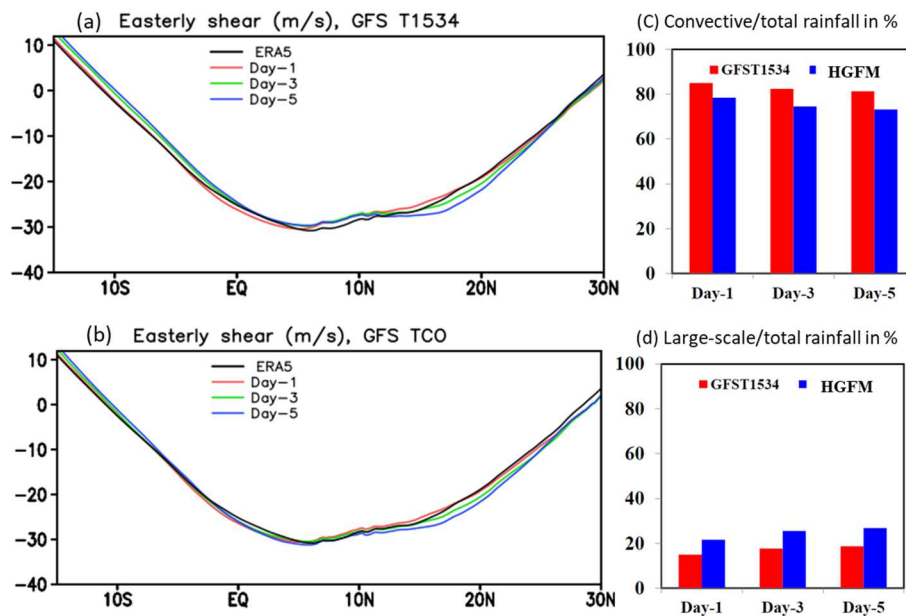
239

240 **Figure 6. Comparison of JJAS mean precipitation (cm/day) and Bias in IMERG data (cm/day) (a) with GFS T1534 (b, c, d) and**
 241 **TCO 1534 (e, f, g) during 2022 over Western ghats region for day-1 day-3 and day-5 lead time.**

242 One of the prominent features of ISM is the vertical shear of zonal wind. Previous studies (Jiang et al., 2004; Abhik et al.,
 243 2013) demonstrated that the vertical easterly wind shear plays a crucial role in inducing baroclinic vorticity ahead of
 244 northward propagation of summer intra-seasonal oscillation. In order to find out the model forecast skill in predicting
 245 realistic easterly wind shear (difference between zonal wind at 200 and 850 hPa) during summer monsoon season of 2022,
 246 the vertical wind shear calculated and represented in Fig. 7a and 7b for GFS T1534 and HGFM respectively over the ISM
 247 region. Figure 7a indicates slightly weaker easterly shear in GFS T1534 compared to ERA5 around 10°N and 0°-15°S for
 248 all lead times. On the contrary, the HGFM is able to predict more realistic easterly wind shear over above regions as shown

249 in the Fig. 7b. It is noticeable that both models overestimate the magnitude of easterly shear around 20° N for Day-3 and
 250 Day-5 lead times.

251 Another key feature about tropical precipitation is almost equipartition of rainfall into convective and stratiform rain.
 252 Therefore, it is important to investigate whether the relative improvement in the precipitation distribution over the ISM
 253 region in HGFM forecasts is contributed by improved convective and large-scale precipitation. The model forecasted
 254 convective and large-scale rainfall ratios are shown in Fig. 7c and 7d respectively. It is noteworthy that the large-scale or
 255 stratiform rainfall plays an important role in the propagation and maintenance of the tropical intraseasonal convection
 256 associated with its top-heavy heating profile (Fu and Wang, 2004; Chattopadhyay et al., 2009; Deng et al., 2015). The
 257 heating profile associated with stratiform rain also helps in large-scale organization of convection (see for example,
 258 Choudhary and Krishnan, 2011, Kumar et al., 2017). The contribution of convective rainfall to the total rainfall appears to be
 259 more than 80 % in GFS T1534 forecast for all lead times (Fig. 7c). Similar overestimation of convective rainfall in GFS
 260 T1534 is reported by Ganai et al. (2021). The observed convective (large-scale) rainfall ratio is around 55 % (45 %) as
 261 shown in Abhik et al. (2017). The HGFM forecast shows relative improvement in predicting convective and large-scale
 262 rainfall ratio compared to GFS T1534 (Fig. 7c and 7d). The decrease (increase) in convective (large-scale) rainfall
 263 contribution to total rain is noted in HGFM forecast. The finer horizontal resolution in HGFM possibly allows for a more
 264 accurate representation of deep convective due to scale-aware representation.

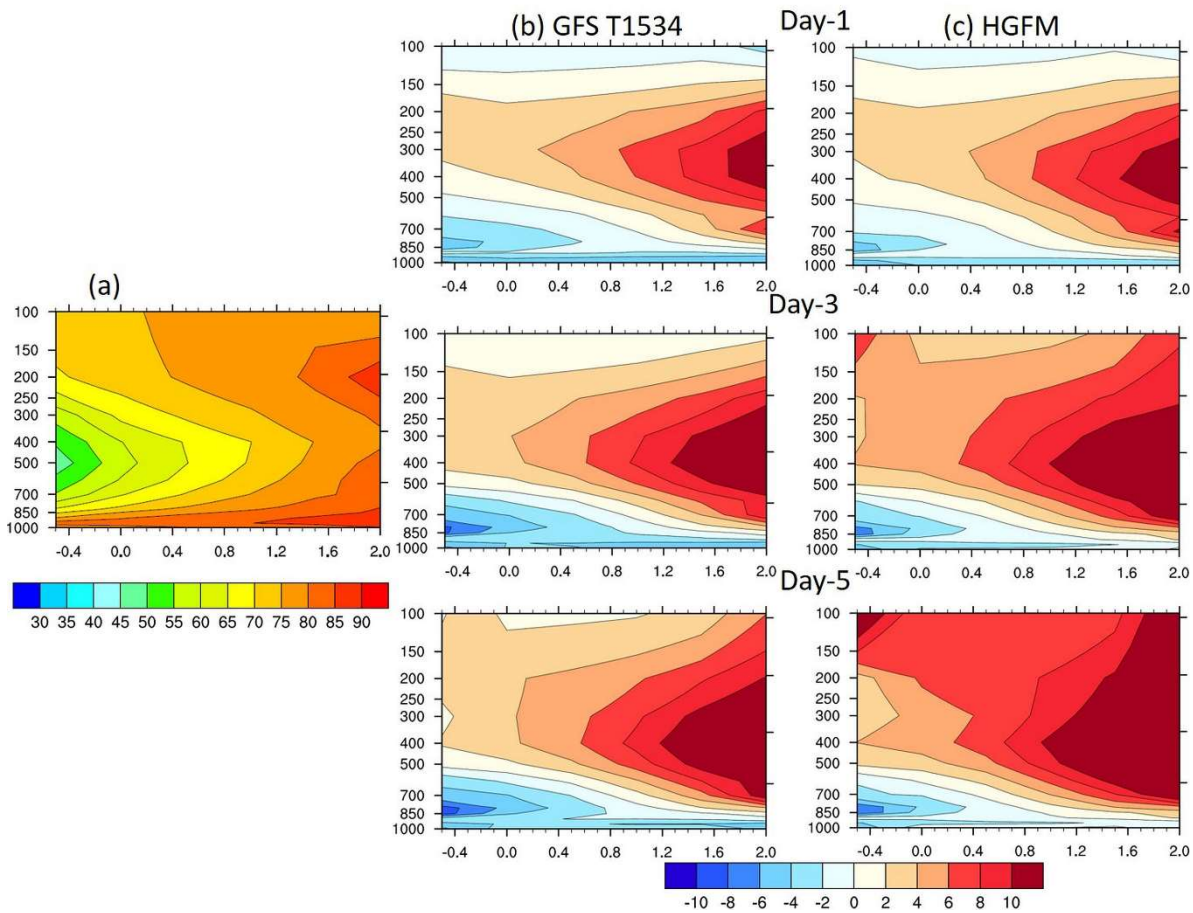


265

266 **Figure 7. Comparison of easterly shear (m/s) from ERA-5 with GFS T1534 (a) and HGFM (b) along with convective/total rainfall**
 267 **(c) and large scale/total rainfall (d) between GFS T1534 and HGFM during JJAS 2022 for day-1 day-3 and day-5 lead time.**

268 To attain further clarity about the model precipitation and moist convective processes, the vertical profile of relative
 269 humidity as a function of rain rate is analyzed for JJAS of 2022 over the ISM region (60° E-100° E, 10° S-30° N). The bias

270 analysis suggests that GFS T1534 has systematically underestimated the lower-level moisture for all lead times (Fig. 8b). It
 271 is consistent with the study by Mukhopadhyay et al. (2019) and Ganai et al. (2021) where they reported similar
 272 underestimation of lower-level moisture over the ISM region in GFS T1534 forecast. In contrast, the HGFM shows relative
 273 improvement in the lower-level moisture distribution, as depicted in Fig. 4c for all lead times. The enhancement of the
 274 lower-level moisture is visible as compared to GFS T1534 forecast. However, the upper troposphere is too moist for both
 275 model forecasts and need further improvement.
 276 It is observed that overall statistics of monsoon rainfall and related convective processes have significantly improved in the
 277 HGFM model. In the next section a case of heavy rainfall is discussed followed by the analysis of recent tropical cyclone
 278 forecasts.
 279

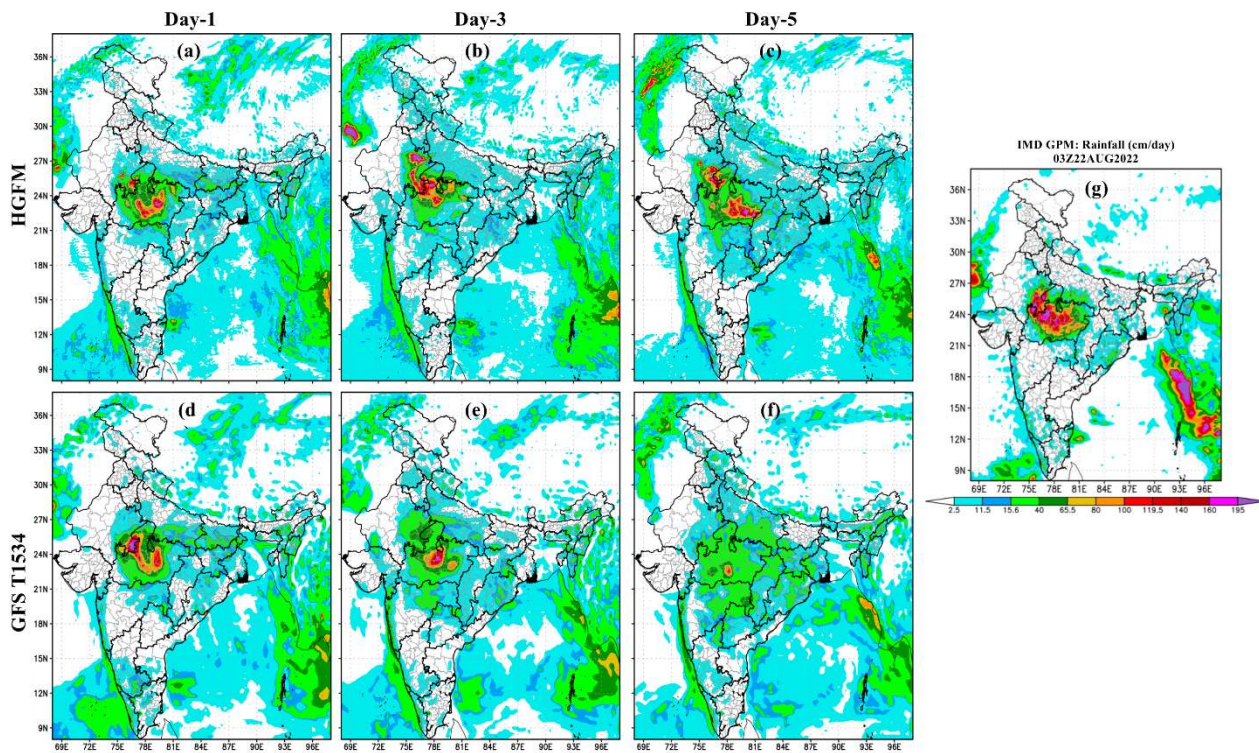


280
 281 **Figure 8. Comparison of Relative humidity (% bias in shaded) vs rain rate (mm/day) over ISM region (60° E-100° E, 10° S-30° N)**
 282 **during JJAS-2022 from ERA-5 and IMERG (a) with GFS T1534 (b) and HGFM (c) during JJAS 2022 for day-1 day-3 and day-5**
 283 **lead time.**

284 **3.5 Evaluation of Heavy Rainfall event**

285 A very heavy rainfall event occurred on 22 August 2022 over central India. This event was well captured by both GFS and
286 HGFM models as compared to the observed rain from IMD-GPM (shown in Fig. 9). Both HGFM (Fig. 9a, b, c) and GFS
287 T1534 (Fig. 9d, e, f) models simulated the heavy rainfall signature compared to IMD GPM (Fig. 9g) on day 1 and day 3
288 forecast. However, a major difference was noted for rainfall intensity and spatial distribution on longer lead time (day 5) in
289 HGFM and GFS T1534. There is an underestimation of rainfall in both the models compared to observations. Whereas the
290 HGFM captures the signal of the occurrence of heavy rainfall even at day 5 lead, which is almost negligible in GFS forecast.
291 Further, the precipitation probability distribution function (PDF) is analyzed (figure not shown) for the JJAS 2022 monsoon.
292 It is found that the HGFM shows better PDF in the very heavy (11.56-20.45 cm/day) and extreme (>20.45 cm/day) rainfall
293 category as compared to GFS T1534.

294

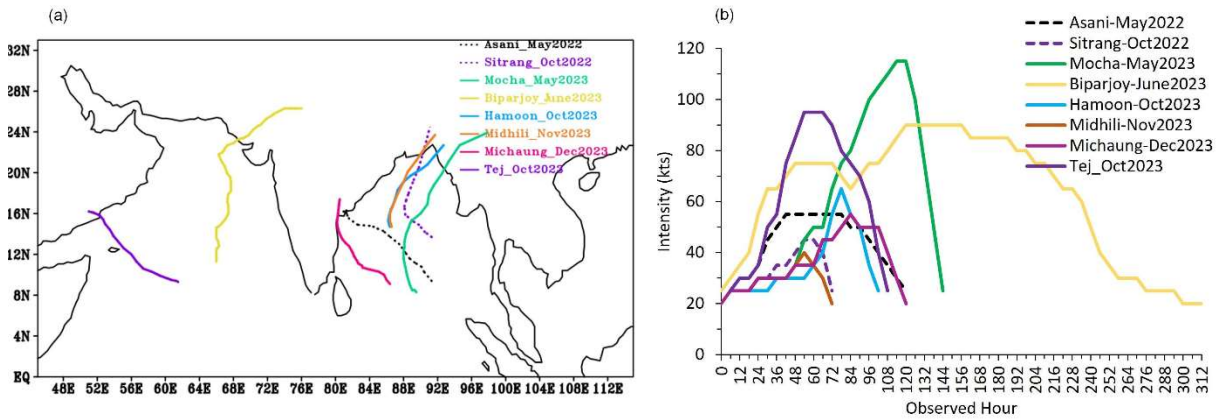


295

296 **Figure 9. Comparison of heavy rainfall event on 22 August 2022 with HGFM (a, b, c), GFS T1534 (d, e, f) for day-1, day-3 and**
297 **day-5 lead times with IMD GPM (g) rainfall.**

298 **3.5 Evaluation of Tropical Cyclone forecast**

299 Total eight named cases of tropical cyclones occurred during 2022 and 2023 (RSMC 2022, RSMC 2023) are considered in
300 the present study. Out of these 8 cases, 2 cyclones formed over the Arabian Sea and 6 cyclones over the Bay of Bengal
301 (BOB). The best track data of track, intensity and landfall is obtained from IMD and referred as observations henceforth in
302 the text. Figure 10 shows observed tracks (Fig. 10a) and observed intensity in terms of Maximum Sustained Wind Speed
303 (MSW Fig. 10b) of the cyclones. The cyclones in the present study have different tracks and various range of severity in
304 terms of intensity over both the basins.
305



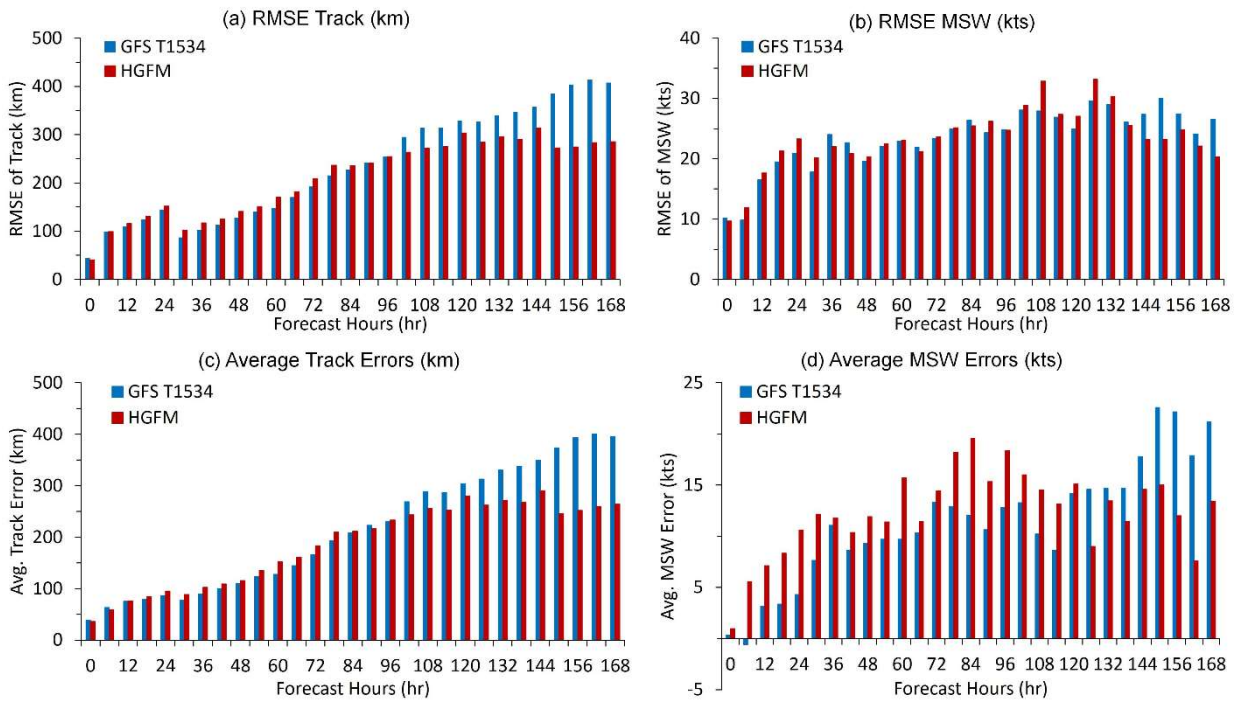
306
307 **Figure 10. a) Observed tracks of the cyclones b) Observed Intensity in terms of Maximum Sustained Wind Speed (kts) during year**
308 **2022-2023.**

309 **3.5.1 Verification of GFS T1534 and HGFM Forecast for tropical cyclone cases during 2022 and 2023**

310 For this verification, the lifetime of the cyclone is considered starting from the depression stage till landfall as per the
311 observation. The total sample includes, minimum four and maximum 10 initial conditions for typical cases depending on the
312 life span of the case. The errors calculated here are averaged for each forecast hour within the sample.
313 The Root Mean Square Error (RMSE) for track and intensity is shown in Fig. 11a and b respectively. Initially upto 4 days,
314 GFS T1534 and HGFM performs equally well but the considerable improvement with HGFM is noted after 4 days in both
315 track and intensity forecast. Figure 11c-d depicts the average track error and average intensity errors for all the cyclones.
316 The average track errors as well as average intensity errors are reduced drastically in HGFM with longer lead hours (4 days
317 or more). Average track errors (average intensity errors) are ~300 km (~20 kts) with 7 days leads in HGFM. The average
318 landfall errors (both position and time) are also evaluated with IMD observations and are shown in Fig. 12. With 4 days lead,
319 average landfall position errors are ~200 km in HGFM and about 250 for GFS 1534. Overall, the landfall position errors are
320 less for HGFM. Remarkable improvements are seen in the average landfall time errors in HGFM throughout the life cycle of
321 cyclones. Overall, the track and intensity forecast are improved with HGFM for longer lead hours (~4 days or more), which

322 is an added advantage for the early warning and mitigation purpose. Here, one of the cyclone cases (cyclone Biparjoy) is
 323 discussed in detail.

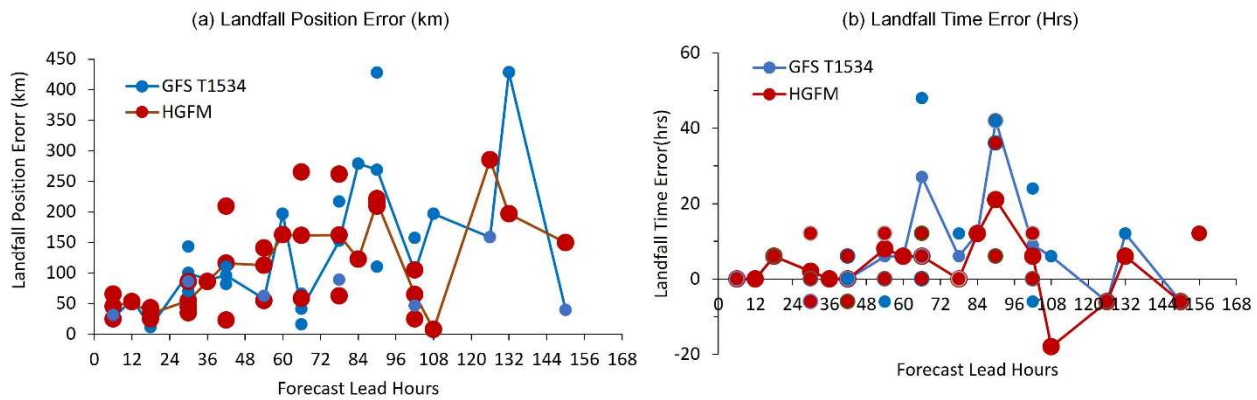
324



325

326 **Figure 11. a) RMSE of Track in km b) RMSE of MSW in kts c) Average Track error (km) d) Average Intensity Errors (kts).**

327



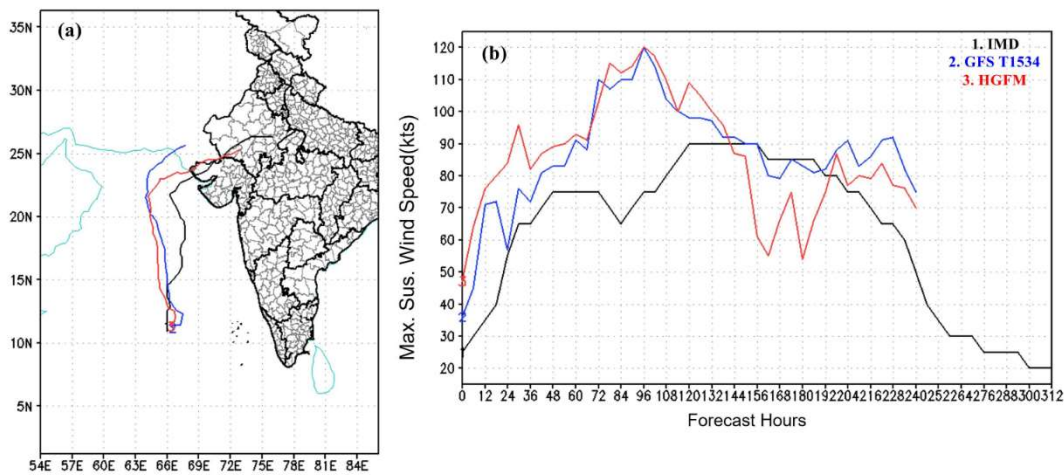
328

329 **Figure 12. a) Average Landfall position errors in km b) Average Landfall time Errors in hours. The continuous lines represent the**
 330 **average errors for GFS T1534 (Blue) and HGFM (Red). The different size of the dots is for making the overlapped points visible.**

331 **3.5.2 A case study - Cyclone Biparjoy**

332 During the monsoon onset of 2023 season, tropical cyclone Biparjoy evolved in the Arabian Sea and hit the north-western
333 state of Gujarat, India. The cyclone Biparjoy lasted for quite a long-time during 6-19 June 2023. As seen in figure 13a, it
334 moved almost parallel to the Indian west coast and had a recurve to finally make landfall over the northern part of Gujarat
335 and adjoining Pakistan. It passed through the rapid intensification during genesis and growing stage on 6 and 7 June This
336 case was particularly challenging for prediction due to combination of recurving track, rapid intensification, slow movement
337 and a long lifespan. The HGFM and GFS T1534 track, and intensity forecast of TC Biparjoy based on 6 June (day of
338 genesis) initial condition, is shown in Fig. 13 a and b along with the best track data from IMD. It is evident that the HGFM
339 predicts a track much closer to the observation compared to GFS T1534. Particularly the recurvature is better captured by
340 HGFM at about 6-7 days lead time. Both the models overestimated the intensity till 120 hrs of forecast and thereafter
341 indicates dissipation phase.

342



343

344

345 **Figure 13. (a) track and (b) intensity variation forecast by GFS T1534, HGFM and as reported by IMD for the case of**
346 **oTropical cyclone Biparjoy over Arabian Sea based on 6 June 2023 initial condition.**

347 To know the robustness of the performance, the verification is carried out for this particular case considering forecast from
348 all the initial conditions (from 6 June 00UTC to 15 June 00UTC, initialized at 24 hrs interval). A comparative analysis of
349 landfall position and landfall time errors with HGFM and GFS T1534 with respect to that reported by IMD has been
350 mentioned in Table 2. It is evident that the landfall position error of the cyclone has been significantly improved by HGFM
351 forecast though the landfall time error appears to be almost equivalent as compared to GFS T1534. Further the average track
352 and intensity error (obtained from total 10 initial conditions) is depicted in Fig. 14a and 14b. It is evident that the HGFM

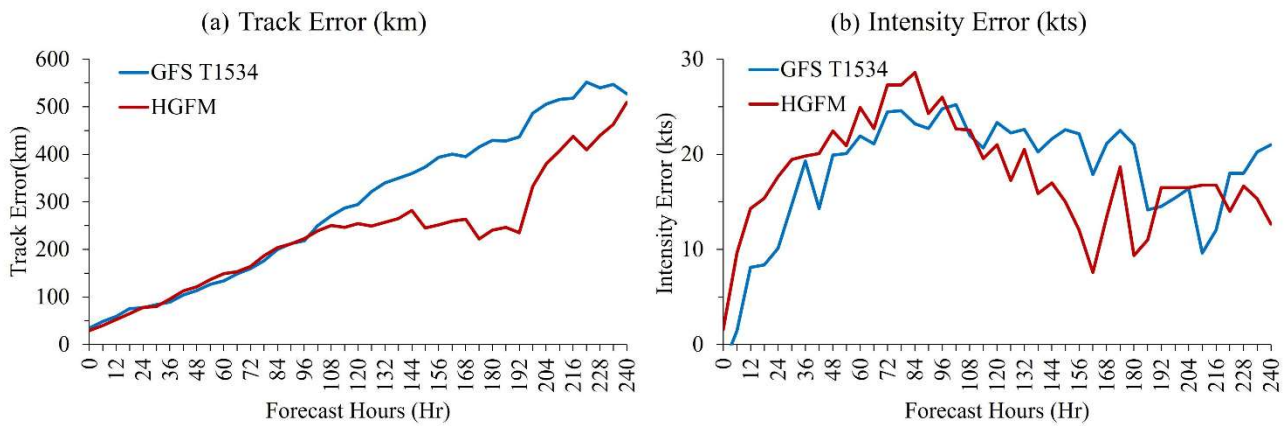
353 produces consistently accurate prediction of track and intensity with lesser error on longer lead while the errors are more or
 354 less same for shorter lead.

355

356 **Table 2. Landfall position (km) and landfall time (hr) errors for the forecasts started with different initial conditions. -ve (+ve)**
 357 **sign indicates early (late) landfall with respect to observed landfall time. The bold numbers indicates the significant improvement**
 358 **in the landfall position errors with HGFM.**

Forecast from landfall (Hr)	Hours Observed	Initial Condition	Landfall Position Error (km)		Landfall Time Error (Hr)	
			GFS T1534	HGFM	GFS T1534	HGFM
228		2023060600	298	57	0	-30
204		2023060700	No Landfall			
180		2023060800	616	201	0	0
156		2023060900	349	197	12	12
132		2023061000	428	197	12	6
108		2023061100	197	7	6	-18
84		2023061200	279	123	12	12
60		2023061300	197	163	6	6
36		2023061400	89	86	0	0
12		2023061500	57	53	0	0

378



379
 380 **Figure 14. a) Average track error and b) average intensity error for the tropical cyclone Biparjoy over Arabian Sea.**

381 **4 Conclusions**

382 For the first time, a version of the GFS model utilizing a new grid structure triangular cubic octahedral (Tco) has been
 383 developed and is being run on an experimental basis for short to medium range weather prediction over the Indian region,
 384 designated as IITM High resolution Global Forecast Model (HGFM). The Tco grid provides a higher resolution over the
 385 tropics, making the model achieve 6.5 km horizontal resolution near the tropics. This higher resolution represents a
 386 substantial leap from the existing Gaussian linear GFS T1534 which maintains a resolution of 12.5 km across the globe. The
 387 KE spectra of 200 hPa zonal wind have also revealed reasonable power by both the model with HGFM showing marginally
 388 better power in the Kolmogorov region indicating fidelity of model structure.

389 It is worth to mention that the present dynamical core using cubic octahedral grid is implemented in ECMWF weather
 390 forecast model since 2016 (Malardel et al., 2016). This has led to a significant increase in forecast accuracy and
 391 computational efficiency in the ECMWF model. In the present study, it is found that the above dynamical core in the GFS
 392 T1534 has improved the orographic rainfall and reduces the Gibbs noise over the mountainous region in addition to
 393 improved precipitation skill over the Indian landmass region. The June-September monsoon rainfall and a case study of
 394 heavy rainfall have been analyzed in detail. The newly developed HGFM shows significantly better skill, particularly in the
 395 longer lead and for heavier rain categories. Rainfall biases over the whole globe appear to be broadly similar between HGFM
 396 and GFS T1534. A case of heavier rainfall in and around central India during the monsoon season has been analysed where
 397 the validation shows a significant gain in forecast lead time by the HGFM compared to GFS T1534. The HGFM captures
 398 rainfall signature at 5 days lead time, when there is hardly any indication in the HGFM model forecast.

399 Several cases of tropical cyclones during 2022 and 2023 were analysed, indicating better performance of HGFM compared
 400 to GFS in predicting tracks and intensity. A case of tropical cyclone Biparjoy has been evaluated in detail based on IMD
 401 observation. It is seen that the HGFM model generates better accuracy of cyclone position in almost all lead time (Table 2)

402 and further the average track error also is found to be much lesser as compared to GFS T1534 in longer lead. However, the
403 errors of both model in average track and intensity are found to be equivalent. This paper highlights the initial results of the
404 newly developed HGFM model and its skill as compared to the operational GFS T1534 model. Subsequently more analyses
405 for many events will be carried out and the model will be made operational for weather forecasts over India. The current set
406 up of the model uses the same physics as the GFS model. However, the HGFM model would require some parameter tuning
407 to optimize the performance of the model and increase its fidelity. The future work will be focused on detailed validation of
408 model simulations with optimal set of physical parameterizations.

409

410

411

412

413

414

415 **Code and Data Availability**

416 The model simulated data used for HGFM and GFS T1534 in the study are available at “TCO model data” by R Phani
417 Murali Krishna, Kumar Siddharth, Athipatta Gopinathan Prajeesh, Malay Ganai, B. Revanth Reddy, Kumar Roy and
418 Parthasarathi Mukhopadhyay, DOI: <https://doi.org/10.5281/zenodo.12569807>. The model code is available at "GFS TCO
419 Model code" by R Phani Murali Krishna, Kumar Siddharth, Athipatta Gopinathan Prajeesh, Parthasarathi Mukhopadhyay.
420 DOI: <https://doi.org/10.5281/zenodo.12526400>

421

422 **Author Contributions**

423 RPK, SK, AGP and PM conceptualised the problem and made necessary changes/modification development of code for
424 Tco and wrote the major part of the Introduction, data, methodology and over all sequences. PB and NW helped during
425 formulation of the Tco grid in GFS and helped in improving the manuscript writing. KR, MG, ST, BRR and TG made all the
426 forecast analysis of monsoon parameters and wrote the respective portion on analyses. RK, MD and SS made the analysis
427 related to cyclone forecast by HGFM model and wrote the section on the cyclone forecast analysis and BRR made the
428 dCAPE analysis and extracted the post processed variables for the analysis.

429

430

431 **Competing interests**

432 The authors declare that they have no conflict of interest.

433

434

435 **Disclaimer**

436

437

438

439 **Acknowledgments**

440 IITM is fully funded by the Ministry of Earth Sciences, Government of India. We would like to thank ECMWF for their
441 support during the model development and for providing the ERA5 data set. We thank NCMRWF for providing the GFS
442 initial conditions used for conducting simulations. We acknowledge Pratyush High Performance Computing at IITM, Pune
443 for providing the computing facility to carry out the simulations. We thank Mr. Vaishak for helping in archiving the data in
444 ARDC server. Authors thank Secretary Ministry of Earth Sciences, Government of India and Director, IITM for support and
445 facilities provided for this study. We thank IMD for providing the IMD-GPM rainfall and cyclone best track data.

446

447

448

449

450

451

452

453

454

455

456

457 **References**

- 458 Abhik, S., Halder, M., Mukhopadhyay, P., Jiang, X., and Goswami, B.N.: A possible new mechanism for northward
459 propagation of boreal summer intraseasonal oscillations based on TRMM and MERRA reanalysis, *Clim. Dyn.*, 40, 1611-
460 1624, <https://doi.org/10.1007/s00382-012-1425-x>, 2013.
- 461 Abhik, S., Krishna, R.P.M., Mahakur, M., Ganai, M., Mukhopadhyay, P., and Dudhia, J.: Revised cloud processes to
462 improve the mean and intraseasonal variability of Indian summer monsoon in climate forecast system: Part 1, *J. Adv.*
463 *Model. Earth. Syst.*, 9(2), 1002-1029, <https://doi.org/10.1002/2016MS000819>, 2017.
- 464 Alpert, J.C., Kanamitsu, M., Caplan, P.M., Sela, J.G., White, G.H., and Kalnay, E.: Mountain induced gravity wave drag
465 parameterization in the NMC medium-range forecast model. In Conference on Numerical Weather Prediction, Baltimore,
466 MD, 8th, 726-733, 1988.
- 467 Arakawa, A. and Schubert, W.H.: Interaction of a cumulus cloud ensemble with the large-scale environment, Part I, *J.*
468 *Atmos. Sci.*, 31(3), 674-701, [https://doi.org/10.1175/1520-0469\(1974\)031<0674:IOACCE>2.0.CO;2](https://doi.org/10.1175/1520-0469(1974)031<0674:IOACCE>2.0.CO;2), 1974.
- 469 Arakawa, A. and Wu, C.M.: A unified representation of deep moist convection in numerical modeling of the atmosphere.
470 Part I, *J. Atmos. Sci.*, 70(7), 1977-1992, <https://doi.org/10.1175/JAS-D-12-0330.1>, 2013.
- 471 Bechtold, P., Köhler, M., Jung, T., Doblas-Reyes, F., Leutbecher, M., Rodwell, M. J., Vitart, F., and Balsamo, G.: Advances
472 in simulating atmospheric variability with the ECMWF model: From synoptic to decadal time-scales, *Q. J. Roy. Meteor.*
473 *Soc.*, 134, 1337–1351, <https://doi.org/10.1002/qj.289>, 2008.
- 474 Chattopadhyay, R., Goswami, B.N., Sahai, A.K., and Fraedrich, K.: Role of stratiform rainfall in modifying the northward
475 propagation of monsoon intraseasonal oscillation, *J. Geophys. Res. Atmos.*, 114(D19),
476 <https://doi.org/10.1029/2009JD011869>, 2009.
- 477 Choudhury, A.D. and Krishnan, R.: Dynamical response of the South Asian monsoon trough to latent heating from
478 stratiform and convective precipitation, *J. Atmos. Sci.*, 68(6), 1347-1363, <https://doi.org/10.1175/2011JAS3705.1>, 2011.
- 479 Chun, H.Y. and Baik, J.J.: Momentum flux by thermally induced internal gravity waves and its approximation for large-scale
480 models, *J. Atmos. Sci.*, 55(21), 3299-3310, [https://doi.org/10.1175/1520-0469\(1998\)055<3299:MFBTII>2.0.CO;2](https://doi.org/10.1175/1520-0469(1998)055<3299:MFBTII>2.0.CO;2), 1998.
- 481 Clough, S.A., Shephard, M.W., Mlawer, E.J., Delamere, J.S., Iacono, M.J., Cady-Pereira, K., Boukabara, S., and Brown,
482 P.D.: Atmospheric radiative transfer modeling: A summary of the AER codes, *J. Quant. Spectrosc. Radiat. Transf.*, 91(2),
483 233-244, <https://doi.org/10.1016/j.jqsrt.2004.05.058>, 2005.

484 Crueger, T., Giorgetta, M.A., Brokopf, R., Esch, M., Fiedler, S., Hohenegger, C., Kornblueh, L., Mauritsen, T., Nam, C.,
485 Naumann, A.K., and Peters, K.: ICON-A, the atmosphere component of the ICON earth system model: II. Model evaluation,
486 *J. Adv. Model. Earth. Syst.*, 10(7), 1638-1662, <https://doi.org/10.1029/2017MS001233>, 2018.

487 Deng, Q., Khouider, B., and Majda, A.J.: The MJO in a coarse-resolution GCM with a stochastic multcloud
488 parameterization, *J. Atmos. Sci.*, 72(1), 55-74. <https://doi.org/10.1175/JAS-D-14-0120.1>, 2015.

489 Deshpande, M., Kanase, R., Krishna, R.P.M., Tirkey, S., Mukhopadhyay, P., Prasad, V.S., Johny, C.J., Durai, V.R., Devi, S.
490 and Mohapatra, M.: Global Ensemble Forecast System (GEFS T1534) evaluation for tropical cyclone prediction over the
491 North Indian Ocean, *Mausam.*, 72(1), 119-128, <https://doi.org/10.54302/mausam.v72i1.123>, 2021.

492 ECMWF IFS DOCUMENTATION—Cy43r1 Operational Implementation Part IV: Physical Processes; ECMWF: Reading,
493 UK, 2016.

494 Fu, X. and Wang, B.: The boreal-summer intraseasonal oscillations simulated in a hybrid coupled atmosphere–ocean
495 model, *Mon. Weather. Rev.*, 132(11), 2628-2649, <https://doi.org/10.1175/MWR2811.1>, 2004.

496 Gadgil, S. and Gadgil, S.: The Indian monsoon, GDP and agriculture, *Econ. polit. Wkly.*, 4887-4895,
497 <https://www.jstor.org/stable/4418949>, 2006.

498 Ganai, M., Tirkey, S., Krishna, R.P.M., and Mukhopadhyay, P.: The impact of modified rate of precipitation conversion
499 parameter in the convective parameterization scheme of operational weather forecast model (GFS T1534) over Indian
500 summer monsoon region, *Atmos. Res.*, 248, 105185, <https://doi.org/10.1016/j.atmosres.2020.105185>, 2021.

501 Giorgetta, M.A., Brokopf, R., Crueger, T., Esch, M., Fiedler, S., Helmert, J., Hohenegger, C., Kornblueh, L., Köhler, M.,
502 Manzini, E., and Mauritsen, T.: ICON-A, the atmosphere component of the ICON earth system model: I. Model description,
503 *J. Adv. Model. Earth. Syst.*, 10(7), 1613-1637, <https://doi.org/10.1029/2017MS001242>, 2018.

504 Han, J. and Pan, H.L.: Revision of convection and vertical diffusion schemes in the NCEP Global Forecast System, *Weather.*
505 *Forecast.*, 26(4), 520-533, <https://doi.org/10.1175/WAF-D-10-05038.1>, 2011.

506 Han, J., Witek, M.L., Teixeira, J., Sun, R., Pan, H.L., Fletcher, J.K., and Bretherton, C.S.: Implementation in the NCEP GFS
507 of a hybrid eddy-diffusivity mass-flux (EDMF) boundary layer parameterization with dissipative heating and modified stable
508 boundary layer mixing, *Weather. Forecast.*, 31(1), 341-352, <https://doi.org/10.1175/WAF-D-15-0053.1>, 2016.

509 Han, J., Wang, W., Kwon, Y.C., Hong, S.Y., Tallapragada, V., and Yang, F.: Updates in the NCEP GFS cumulus convection
510 schemes with scale and aerosol awareness, *Weather. Forecast.*, 32(5), 2005-2017, [https://doi.org/10.1175/WAF-D-17-](https://doi.org/10.1175/WAF-D-17-0046.1)
511 0046.1, 2017.

512 Held, I.M. and Suarez, M.J.: A proposal for the intercomparison of the dynamical cores of atmospheric general circulation
513 models, *Bull. Am. Meteorol. Soc.*, 75(10), 1825-1830, [https://doi.org/10.1175/1520-](https://doi.org/10.1175/1520-0477(1994)075<1825:APFTIO>2.0.CO;2)
514 0477(1994)075<1825:APFTIO>2.0.CO;2, 1994.

515 Hersbach, H. and Dee, D.: ERA5 reanalysis is in production. ECMWF Newsletter No. 147,
516 ECMWF, Reading, United Kingdom, 7, [http://www.ecmwf.int/sites/default/files/elibrary/2016/16299-newsletter-no147-spring-](http://www.ecmwf.int/sites/default/files/elibrary/2016/16299-newsletter-no147-spring-2016.pdf)
517 2016.pdf, 2016.

518 Hoffman, R.N., Kumar, V.K., Boukabara, S.A., Ide, K., Yang, F., and Atlas, R.: Progress in forecast skill at three leading
519 global operational NWP centers during 2015–17 as seen in summary assessment metrics (SAMs), *Weather. Forecast.*, 33(6),
520 1661-1679, <https://doi.org/10.1175/WAF-D-18-0117.1>, 2018.

521 Huffman, G.J., Stocker, E.F., Bolvin, D.T., Nelkin, E.J., and Tan, J.: GPM IMERG Final Precipitation L3 Half Hourly 0.1
522 degree x 0.1 degree V06, Greenbelt, MD, Goddard Earth Sciences Data and Information Services Center (GES DISC),
523 Accessed: 20 March 2023, doi:10.5067/GPM/IMERG/3B-HH/06, 2019.

524 Iacono, M.J., Mlawer, E.J., Clough, S.A., and Morcrette, J.J.: Impact of an improved longwave radiation model, RRTM, on
525 the energy budget and thermodynamic properties of the NCAR community climate model, CCM3, *J. Geophys. Res. Atmos.*,
526 105(D11), 14873-14890, <https://doi.org/10.1029/2000JD900091>, 2000.

527 Jiang, X., Li, T., and Wang, B.: Structures and mechanisms of the northward propagating boreal summer intraseasonal
528 oscillation, *J. Clim.*, 17(5), 1022-1039, [https://doi.org/10.1175/1520-0442\(2004\)017<1022:SAMOTN>2.0.CO;2](https://doi.org/10.1175/1520-0442(2004)017<1022:SAMOTN>2.0.CO;2), 2004.

529 Kanase, R., Tirkey, S., Deshpande, M., Krishna, R.P.M., Johny, C.J., Mukhopadhyay, P., Iyengar, G., and Mohapatra, M.:
530 Evaluation of the Global Ensemble Forecast System (GEFS T1534) for the probabilistic prediction of cyclonic disturbances
531 over the North Indian Ocean during 2020 and 2021, *J. Earth. Sys. Sci.*, 132-143, [https://doi.org/10.1007/s12040-023-02166-](https://doi.org/10.1007/s12040-023-02166-2)
532 2, 2023.

533 Kim, Y.J. and Arakawa, A.: Improvement of orographic gravity wave parameterization using a mesoscale gravity wave
534 model, *J. Atmos. Sci.*, 52(11), 1875-1902, [https://doi.org/10.1175/1520-0469\(1995\)052<1875:IOOGWP>2.0.CO;2](https://doi.org/10.1175/1520-0469(1995)052<1875:IOOGWP>2.0.CO;2), 1995.

535 Kinter, J. L., III, Cash, B., Achuthavarier, D., Adams, J., Altshuler, E., Dirmeyer, P., Doty, B., Huang, B., Jin, E. K., Marx,
536 L., Manganello, J., Stan, C., Wakefield, T., Palmer, T., Hamrud, M., Jung, T., Miller, M., Towers, P., Wedi, N., Satoh, M.,
537 Tomita, H., Kodama, C., Nasuno, T., Oouchi, K., Yamada, Y., Taniguchi, H., Andrews, P., Baer, T., Ezell, M., Halloy, C.,
538 John, D., Loftis, B., Mohr, R., & Wong, K.: Revolutionizing Climate Modeling with Project Athena: A Multi-Institutional,
539 International Collaboration. *Bull. Am. Meteorol. Soc.*, 94(2), 231-245. <https://doi.org/10.1175/BAMS-D-11-00043.1>, 2013.

540 Kumar, S., Arora, A., Chattopadhyay, R., Hazra, A., Rao, S.A., and Goswami, B.N.: Seminal role of stratiform clouds in
541 large-scale aggregation of tropical rain in boreal summer monsoon intraseasonal oscillations, *Clim. Dyn.*, 48, 999-1015,
542 <https://doi.org/10.1007/s00382-016-3124-5>, 2017.

543 Kumar, S., Phani, R., Mukhopadhyay, P., and Balaji, C.: Does increasing horizontal resolution improve seasonal prediction
544 of Indian summer monsoon?: A climate forecast system model perspective, *Geophys. Res. Lett.*, 49(7), e2021GL097466,
545 <https://doi.org/10.1029/2021GL097466>, 2022.

546 Li, J., Yu, R., Yuan, W., Chen, H., Sun, W. and Zhang, Y.: Precipitation over East Asia simulated by NCAR CAM5 at
547 different horizontal resolutions. *J. Adv. Model. Earth. Syst.*, 7(2), 774-790, <https://doi.org/10.1002.2014MS000414>,
548 2015. Lott, F. and Miller, M.J.: A new subgrid-scale orographic drag parametrization: Its formulation and testing, *Q. J. R.*
549 *Meteorol. Soc.*, 123(537), 101-127, <https://doi.org/10.1002/qj.49712353704>, 1997.

550 Magnusson, L. and Källén, E.: Factors influencing skill improvements in the ECMWF forecasting system, *Mon. Weather.*
551 *Rev.*, 141(9), 3142-3153, <https://doi.org/10.1175/MWR-D-12-00318.1>, 2013.

552 Majewski, D., Liermann, D., Prohl, P., Ritter, B., Buchhold, M., Hanisch, T., Paul, G., Wergen, W. and Baumgardner, J.:
553 The operational global icosahedral-hexagonal gridpoint model GME: description and high resolution tests, *Mon. Wea. Rev.*,
554 130, 319– 338, [https://doi.org/10.1175/1520-0493\(2002\)130<0319:TOGIHG>2.0.CO;2](https://doi.org/10.1175/1520-0493(2002)130<0319:TOGIHG>2.0.CO;2), 2002.

555 Malardel, S., N, Wedi., W, Deconinck., M, Diamantakis., C, Kühnlein., G, Mozdzyński., M, Hamrud. and P,
556 Smolarkiewicz.: A new grid for the IFS, ECMWF Newsletter No. 146, 23–28, 2016.

557 Mitra, A.K., Prakesh, S., Imranali, M.M., Pai, D.S. and Srivastava, A.K.: Daily merged satellite gauge real-time rainfall
558 dataset for Indian Region, *Vayumandal*, 40(1-4), 33-43, 2014.

559 Miura, H., Satoh, M., Nasuno, T., Noda, A. T., and Oouchi, K.: A Madden-Julian Oscillation event realistically simulated by
560 a global cloud-resolving model, *Sci.*, 318(5857), 1763–1765, <https://doi.org/10.1126/science.1148443>, 2007.

561 Molod, A., Takacs, L., Suarez, M., and Bacmeister, J.: Development of the GEOS-5 atmospheric general circulation model:
562 Evolution from MERRA to MERRA2, *Geosci. Model. Dev.*, 8(5), 1339-1356, <https://doi.org/10.5194/gmd-8-1339-205>,
563 2015.

564 Mukhopadhyay, P., Prasad, V.S., Krishna, R.P.M., Deshpande, M., Ganai, M., Tirkey, S., Sarkar, S., Goswami, T., Johny,
565 C.J., Roy, K., and Mahakur, M.: Performance of a very high-resolution global forecast system model (GFS T1534) at 12.5
566 km over the Indian region during the 2016–2017 monsoon seasons, *J. Earth. Sys. Sci.*, 128, 1-18,
567 <https://doi.org/10.1007/s12040-019-1186-6>, 2019.

568 Mukhopadhyay, P., Bechtold, P., Zhu, Y., Murali Krishna, R.P., Kumar, S., Ganai, M., Tirkey, S., Goswami, T., Mahakur,
569 M., Deshpande, M., and Prasad, V.S.: Unraveling the mechanism of extreme (more than 30 sigma) precipitation during
570 August 2018 and 2019 over Kerala, India, *Weather. Forecast.*, 36(4), 1253-1273, <https://doi.org/10.1175/WAF-D-20-0162.1>,
571 2021.

572 Nastrom, G.D. and Gage, K.S.: A climatology of atmospheric wavenumber spectra of wind and temperature observed by
573 commercial aircraft, *J. Atmos. Sci.*, 42, 950–960, [https://doi.org/10.1175/1520-0469\(1985\)042<0950:ACOAWS>2.0.CO;2](https://doi.org/10.1175/1520-0469(1985)042<0950:ACOAWS>2.0.CO;2),
574 1985.

575 Pan, H.L. and Wu, W.S.: Implementing a mass flux convection parameterization package for the NMC medium-range
576 forecast model. <https://repository.library.noaa.gov/view/noaa/11429>, 1995.

577 Prakash, S., Mitra, A.K., Momin, I.M., Rajagopal, E.N., Milton, S.F., and Martin, G.M.: Skill of short-to medium-range
578 monsoon rainfall forecasts from two global models over India for hydro-meteorological applications, *Meteorol. Appl.*, 23(4),
579 574-586, <https://doi.org/10.1002/met.1579>, 2016.

580 Prasad, V.S., Mohandas, S., Gupta, M.D., Rajagopal, E.N., and Dutta, S.K.: Implementation of upgraded global forecasting
581 systems (T382L64 and T574L64) at NCMRWF, In NCMRWF Technical Report, 1-72, 2011.

582 Prasad, V.S., Mohandas, S., Dutta, S.K., Gupta, M.D., Iyengar, G.R., Rajagopal, E.N., and Basu, S.: Improvements in
583 medium range weather forecasting system of India, *J. Earth. Sys. Sci.*, 123, 247-258, <https://doi.org/10.1007/s12040-014->
584 0404-5, 2014.

585 Prasad, V.S., Johny, C.J., Mali, P., Singh, S.K., and Rajagopal, E.N.: Global retrospective analysis using NGFS for the
586 period 2000–2011, *Current Sci.*, 370-377, <https://www.jstor.org/stable/24912364>, 2017.

587 Rajendran, K., Kitoh, A., Mizuta, R., Sajani, S., and Nakazawa, T.: High-resolution simulation of mean convection and its
588 intraseasonal variability over the tropics in the MRI/JMA 20-km mesh AGCM, *J. Clim.*, 21(15), 3722-3739,
589 <https://doi.org/10.1175/2008JCLI1950.1>, 2008.

590 Rao, S.A., Goswami, B.N., Sahai, A.K., Rajagopal, E.N., Mukhopadhyay, P., Rajeevan, M., Nayak, S., Rathore, L.S.,
591 Sheno, S.S.C., Ramesh, K.J., and Nanjundiah, R.S.: Monsoon mission: a targeted activity to improve monsoon prediction
592 across scales, *Bull. Am. Meteorol. Soc.*, 100(12), 2509-2532, <https://doi.org/10.1175/BAMS-D-17-0330.1>, 2019.

593 Raymond, D. J.: Convection in the east Pacific Intertropical Convergence Zone, *Geophys. Res. Lett.*, 44, 562-568,
594 [doi:10.1002/2016GL071554](https://doi.org/10.1002/2016GL071554), 2017.

595 RSMC Report, Report on Cyclonic disturbances over North Indian Ocean during 2022, India Meteorological Department,
596 https://rsmcnewdelhi.imd.gov.in/report.php?internal_menu=Mjc=

597 RSMC Report, Report on Cyclonic disturbances over North Indian Ocean during 2023, India Meteorological Department,
598 https://rsmcnewdelhi.imd.gov.in/report.php?internal_menu=Mjc=

599 Satoh, M., Tomita, H., Miura, H., Iga, S., and Nasuno, T.: Development of a global cloud resolving model-a multi-scale
600 structure of tropical convections, *J. Earth. Simul.*, 3, 11-19, 2005.

601 Satoh, M., Stevens, B., Judt, F., Khairoutdinov, M., Lin, S.J., Putman, W.M., and Düben, P.: Global cloud-resolving models,
602 *Curr. Clim. Change Rep.*, 5, 172-184, <https://doi.org/10.1007/s40641-019-00131-0>, 2019.

603 Skamarock, W.C.: Evaluating Mesoscale NWP Models Using Kinetic Energy Spectra, *Mon. Weather. Rev.*, 132,3019–3032,
604 <https://doi.org/10.1175/MWR2830.1>, 2004.

605 Skamarock, W.C., Klemp, J.B., Duda, M.G., Fowler, L.D., Park, S.H., and Ringler, T.D.: A multiscale nonhydrostatic
606 atmospheric model using centroidal Voronoi tessellations and C-Grid staggering, *Mon. Weather. Rev.*, 140(9), 3090–
607 3105, <https://doi.org/10.1175/MWR-D-11-00215.1>, 2012.

608 Staniforth, A. and Thuburn, J.: Horizontal grids for global weather and climate prediction models: a review. *Q. J. R.*
609 *Meteorol. Soc.*, 138(662), 1-26, <https://doi.org/10.1002/qj.958>, 2012.

610 Stephens, G.L., L'Ecuyer, T., Forbes, R., Gettelmen, A., Golaz, J.C., Bodas-Salcedo, A., Suzuki, K., Gabriel, P., and Haynes,
611 J.: Dreary state of precipitation in global models, *J. Geophys. Res. Atmos.*, 115(D24), <https://doi.org/10.1029/2010JD014532>,
612 2010.

- 613 Sundqvist, H., Berge, E., and Kristjánsson, J.E.: Condensation and cloud parameterization studies with a mesoscale
614 numerical weather prediction model, *Mon. Weather. Rev.*, 117(8), 1641-1657, [https://doi.org/10.1175/1520-0493\(1989\)117<1641:CACPSW>2.0.CO;2](https://doi.org/10.1175/1520-0493(1989)117<1641:CACPSW>2.0.CO;2), 1989.
- 616 Watson, P.A., Berner, J., Corti, S., Davini, P., von Hardenberg, J., Sanchez, C., Weisheimer, A., and Palmer, T.N.: The
617 impact of stochastic physics on tropical rainfall variability in global climate models on daily to weekly time scales, *J.*
618 *Geophys. Res. Atmos.*, 122(11), 5738-5762, <https://doi.org/10.1002/2016JD026386>, 2017.
- 619 Wedi, N.P., Polichtchouk, I., Dueben, P., Anantharaj, V.G., Bauer, P., Boussetta, S., Browne, P., Deconinck, W., Gaudin,
620 W., Hadade, I., and Hatfield, S.: A baseline for global weather and climate simulations at 1 km resolution, *J. Adv. Model.*
621 *Earth. Syst.*, 12(11), e2020MS002192, <https://doi.org/10.1029/2020MS002192>, 2020.
- 622 Westra, S., Fowler, H.J., Evans, J.P., Alexander, L.V., Berg, P., Johnson, F., Kendon, E.J., Lenderink, G., and Roberts, N.:
623 Future changes to the intensity and frequency of short-duration extreme rainfall, *Rev. Geophys.*, 52(3), 522-555,
624 <https://doi.10.1002/2014RG000464>, 2014.
- 625 Zhang, G.J.: Convective quasi-equilibrium in the tropical western Pacific: Comparison with midlatitude continental
626 environment, *J. Geophys. Res. Atmos.*, 108(D19), <https://doi.org/10.1029/2003JD003520>, 2003.
- 627 Zhao, Q. and Carr, F.H.: A prognostic cloud scheme for operational NWP models, *Mon. Weather. Rev.*, 125(8), 1931-1953,
628 [https://doi.org/10.1175/1520-0493\(1997\)125<1931:APCSFO>2.0.CO;2](https://doi.org/10.1175/1520-0493(1997)125<1931:APCSFO>2.0.CO;2), 1997.